International Journal of Rock Mechanics & Mining Sciences 81 (2016) 47–61

Contents lists available at ScienceDirect

International Journal of Rock Mechanics & Mining Sciences

journal homepage: www.elsevier.com/locate/ijrmms

Application of Synthetic Rock Mass modeling to veined core-size samples

Javier A. Vallejos [a,*], Kimie Suzuki [a], Andrés Brzovic [b], Diego Mas Ivars [c]

[a] Department of Mining Engineering and Advanced Mining Technology Center, University of Chile, Santiago, Chile
[b] Codelco División El Teniente, Rancagua, Chile
[c] Itasca Consultants AB, Kista, Sweden

ARTICLE INFO

Article history:
Received 15 July 2014
Received in revised form
29 October 2015
Accepted 6 November 2015
Available online 21 November 2015

Keywords:
Synthetic Rock Mass
Numerical modeling
Veined rock
Laboratory samples

ABSTRACT

Rock masses of the primary copper ore at the El Teniente mine fail mainly through the infill of preexisting veins during the caving processes, especially through those composed of less than 35% hard minerals (quartz and pyrite). In this study, the Synthetic Rock Mass (SRM) approach is used to reproduce the results of ten uniaxial compression tests on veined core-size samples of El Teniente Mafic Complex (CMET) lithology, from El Teniente mine, Codelco-Chile. At the scale of the tested samples it is observed that veins composed mostly of quartz dominate the failure process. The developed methodology considers generating a deterministic Discrete Fracture Network (DFN) based on the veins mapped at the surface of each core sample. Then, the micro-parameters of the Bonded Particle Model (BPM) are calibrated to represent the macro-parameters of the average block of intact rock within all samples. Next, the micro-parameters of the Smooth-Joint Contact Model (SJCM), which represent the mechanical properties of veins, are calibrated to reproduce the stress–strain curves and the failure modes of the veined core-size samples measured during the laboratory tests. Results show that the SRM approach is able to reproduce the behavior of the veined rock samples under uniaxial loading conditions. The strength and stiffness of veins, as well as the vein network, have an important impact on the deformability and global strength of the synthetic samples. Contrary to what was observed in the laboratory tests, synthetic samples failed mainly through weak veins. This result is expected in the modeling given that anhydrite veins are considered weaker than quartz veins. Further research is required to completely understand the impact of veins on the behavior of rock masses.

1. Introduction

Discontinuities are structural breaks characterized by their geometry and strength properties, which may or may not impact the rock block and rock mass strength. In the case of El Teniente mine, the largest known copper–molybdenum deposit in the world,[1] discontinuities recognized within the primary copper ore are mainly widely spaced faults[2] and a stockwork formed of a high frequency network of small veins characterized by an intermediate to high tensile strength.[3,4] Therefore, rock masses of the primary copper ore at the El Teniente mine can be conceived of as an assemblage of intact rock blocks bounded by veins.[5] Traditional rock mass classification systems are not well suited to represent these rock masses,[3] mainly because these methodologies consider mainly open joints[6–8] and do not take into account the multiple mineral ensembles of the vein infill.[9] Furthermore, the ability of rock mass classification systems for considering strength anisotropy, scale effect, and post-peak response is limited. Numerical modeling can improve the understanding of the rock mass behavior and rock mass disassembly during caving propagation; therefore, improve rock mass characterization.[5]

The Synthetic Rock Mass (SRM) approach has been implemented in PFC^{3D} 4.0 software[10] and uses the interface SRMLab 1.7.[11] PFC^{3D} solves the problem by using the explicit formulation of the Distinct Element Method,[12] where particles are rigid spherical bodies joined by deformable contacts. The complex interactions among the particles define the macroscopic response of such an assembly. The input parameters cannot be measured directly with conventional laboratory tests. Therefore, a calibration process is required, that is, the micro-parameters are chosen to match the laboratory test response of the rock material. A trial-and-error approach is the basic way to define a suitable set of micro-parameters.[10]

The SRM technique can be used as a virtual laboratory to perform numerical experiments in order to represent in a qualitative and quantitative manner the mechanical behavior of a rock

* Corresponding author.
E-mail address: javallej@ing.uchile.cl (J.A. Vallejos).

http://dx.doi.org/10.1016/j.ijrmms.2015.11.003
1365-1609/

mass.[13–15] The main potential is to simulate fracture propagation and slip on discontinuities in a rock mass under selected loading conditions. The SRM method has been validated through comparison of micro-seismicity, fragmentation, and yielding in SRM samples with rock mass response observed in cave mining operations.[13,16] Other uses of the technique are related to study the effect of sample size on rock mass strength[15,17–19] and the derivation of equivalent rock mass properties.[20] Few studies have performed rigorous comparisons of SRM tests with well-documented laboratory tests. Existing studies in the area have only considered non-cohesive joints and weak intact rock.[21] These studies have concluded that the SRM approach is able to reproduce the UCS and failure mode of jointed samples under uniaxial loading conditions. Further improvement and validation are still required, especially under controlled conditions that can be easily simulated.

Several studies have been carried out by the El Teniente mine to estimate vein strength and stiffness[22–24] and their influence on the disassembly of the rock mass.[3] These studies enable to evaluate the ability of the SRM methodology to reproduce direct shear tests on chalcopyrite vein[25] and uniaxial compression tests including the explicit vein network of laboratory size samples.[26] Even though there is not enough evidence to validate the SRM technique with field cases, simulations of large-scale samples have been performed. These results are compared with estimations based on classification systems and other numerical model estimations [23,27–29].

The objective of this study is to apply the SRM technique to reproduce the behavior of laboratory scale samples from El Teniente mine (Codelco-Chile) under uniaxial loading conditions. Samples are from a veined rock mass, specifically El Teniente Mafic Complex (CMET) unit. This paper first reviews the main aspects and limitations of the components of the SRM modeling technique. Next, the input and validation data are presented, which are obtained from laboratory tests developed for this study and from the El Teniente mine laboratory tests database. Subsequently, Section 4 presents the procedure used to calibrate each component of the model, and how they are combined to calibrate the SRM sample. Finally, results from the calibration are presented and discussed. It is expected that these results provide a fundamental understanding of the behavior of veins in a synthetic sample, particularly with the purpose of its application to larger samples.

2. Synthetic Rock Mass (SRM)

The SRM model represents the intact rock as an assembly of bonded particles using the Bonded Particle Model (BPM),[30] and an embedded Discrete Fracture Network (DFN) in SRM samples to represent discontinuities. Each discontinuity is modeled explicitly using the Smooth-Joint Contact model (SJCM).[31] Fig. 1 shows the main components of a SRM sample. The following paragraphs present the main aspects and limitations of each model.

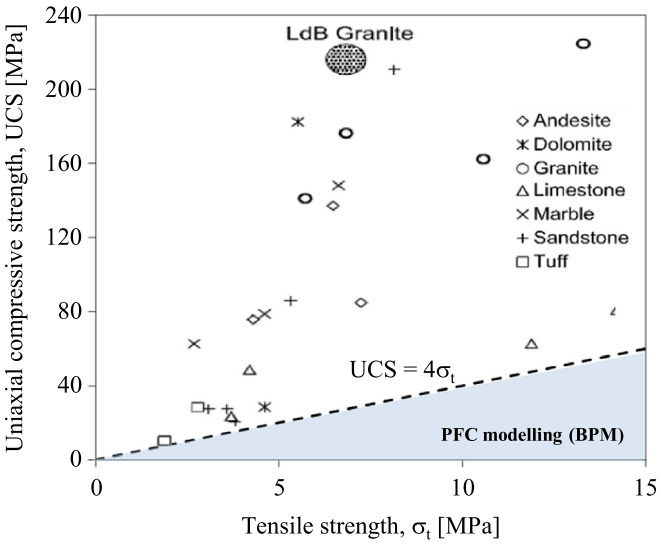

Fig. 2. Comparison between compressive strength and tensile strength for different rock types.[39]

Conventional PFC^{3D} modeling of intact rock considers the standard BPM,[30] which has two main limitations. First, the reproduced compressive to tensile strength ratio is lower than 4. Fig. 2 presents a summary of the uniaxial compressive and tensile strengths for different rock types,[32] indicating that PFC^{3D} could not represent them properly. Second, the failure envelope is linear providing friction angles lower than 30°. Some options to solve this problem are changing the particle size distribution, so the porosity is reduced,[33,34] or changing the particle shape by using clusters[30] or clumps.[35] New models have been created to overcome these limitations: an enhanced version of BPM[36] and the Flat Joint Model.[37,38] The present study uses the enhanced BPM, a parallel-bond refinement, to represent intact rock behavior.

In general, BPM represents the mechanical behavior of a collection of spherical grains joined by cement. The particle diameters satisfy a uniform particle size distribution bounded by D_{min} and D_{max}, where D_{max}/D_{min} controls the packing fabric. Two models characterize the BPM: the Particle Contact Model and the Parallel Bond Model. The first model is defined by the following micro-parameters: Young's modulus (E_c), ratio between normal and shear stiffness ($\frac{k^n}{k^s}$), density (ρ), and friction coefficient (μ), while the second model by: the normal strength ($\bar{\sigma}_c$), cohesion ($\bar{c}$), friction angle ($\bar{\phi}$), Young's modulus ($\bar{E}_c$), ratio between normal and shear stiffness ($\frac{\bar{k}^n}{\bar{k}^s}$), and radius multiplier parameter used to set the parallel-bond radius ($\bar{\lambda}$). The main differences between the standard and the enhanced BPM are in the Parallel Bond Model. The enhanced version considers that all loads are carried by the parallel-bond until it breaks, and then transferred to the contacts

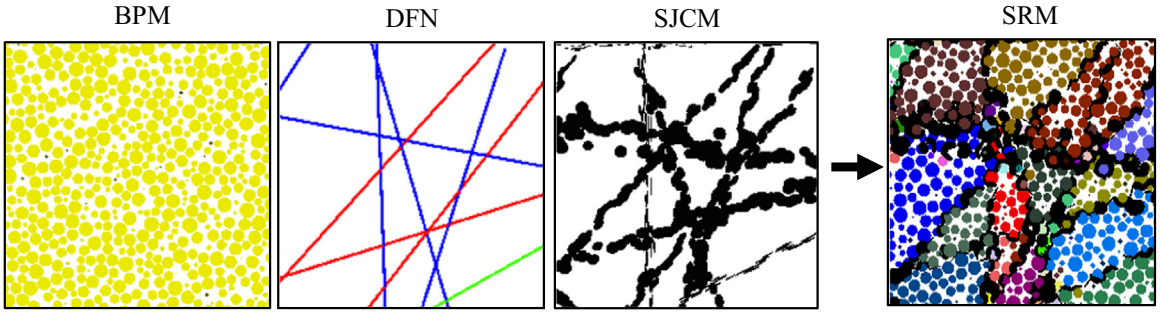

Fig. 1. Synthetic Rock Mass basic components.

Table 1
Summary of the main characteristics of each veined core-size sample.

Sample	Diameter [mm]	Height [mm]	Weight [gr]	Number of veins		
				Anhydrite	Chalcopyrite	Quartz
NNM-04-1	49.7	101.3	554.5	4	0	12
NNM-07-4	49.7	103.7	568.2	2	0	11
NNM-09-1	49.8	104.6	570.3	2	0	12
NNM-09-4	49.8	105.6	581.4	5	2	11
NNM-16-1	52.3	109.4	681.7	4	2	11
NNM-21-1	49.8	104.7	578.1	3	1	10
NNM-21-3	49.8	105.8	584.6	4	1	6
NNM-21-4	49.8	104.0	569.3	4	0	9
NNM-22-1	49.9	104.9	576.1	3	1	7
NNM-22-2	49.9	106.2	581.5	5	2	11
Total	–	–	–	36	9	100
Min.	49.7	101.3	554.5	2	0	6
Max.	52.3	109.4	681.7	5	2	12
Mean	50.1	105.0	584.6	3.6	0.9	10.0
s.d.	0.8	2.1	35.2	1.1	0.9	2.1

(B_{pb_all}=true). Also, a moment contribution factor ($\bar{\beta}$=0) is included. A more detailed explanation of both BPM can be found in Refs. 30 and 36.

The geometric and mechanical characteristics of joints have an influence on the anisotropy and scale effect presented by some rock mass properties. DFN modeling is based on a representation of the discontinuity network within a geotechnical domain using statistical distributions to describe the orientation, persistence, and spatial location. In the case of El Teniente rock mass, veins instead of discontinuities have to be modeled. Even though DFN is a valuable tool, models are limited by the uncertain fracture system geometry and, in general, can only be approximately estimated. The model has some shortcomings based on basic assumptions. As veins are considered as planar and circular discs, parameters such as the thickness, roughness and heterogeneities of the discontinuities, and intact rock bridges are not explicitly considered. However, they are implicitly accounted for in the calibration process by matching laboratory test results.

Interfaces can be represented in PFC^{3D} by assigning new micro-parameters to the bonds through a predefined plane[39] or by using the SJCM.[31] The SJCM simulates the behavior of a frictional or bonded joint at all contacts between particles at opposite sides of the joint. However, the SJCM have the following limitations: (1) reduces the influence of the roughness and does not consider the geometric variation explicitly,[40] (2) considers that the normal stiffness is the same in tension and compression stress paths, (3) does not consider the dependence of normal and shear stiffness with confinement, and (4) generates interlocking when the shear displacement is greater than the minimum diameter of the particles.[41] A more realistic model may include the roughness profile,[42,43] The micro-parameters of the SJCM are the normal and shear stiffness per unit area ($\bar{k}_n$ and $\bar{k}_s$), radius multiplier ($\bar{\lambda}$), friction coefficient (μ), dilation angle (Ψ), bond mode (non-bonded or bonded), tensile strength (σ_c), cohesion (c_b), and bond friction angle (ϕ_b). A more detailed explanation of the SJCM can be found in Refs. 10,31.

3. Data

The main rock types at the El Teniente mine are described as mafic intrusive complex (andesite), felsic intrusive rocks (dacite and diorite), and hydrothermal breccia (Braden breccia). The most abundant rock is denominated as the El Teniente Mafic Complex (CMET) and hosts 80% of the copper mineralization.[1] Two different sectors are distinguished, because they have different alteration zones and structural domains,[5] the west part is called the hanging wall (HW) and the east part is called the footwall (FW). The main difference of this rock mass from the other ones is the mineralogical infill of the veins, which agrees with the definition of the orebody's hydrothermal alteration zones.[4] The infill observed in veins within rock masses at the El Teniente mine can be studied by a quantitative estimation using the percentage of hard infilling represented by quartz or pyrite. For example, the average vein within units like CMET HW or dacite has more than 60% hard infilling, while an average vein within units like CMET FW or diorite had more than 30% hard infilling only. Different mineralogical compositions should show different rock samples behavior after being tested.

The following section includes a summary of the geological characterization of the veins visible at the surface of the samples from the CMET HW lithology tested in the laboratory, and the parameters from the El Teniente mine database describing the intact rock and veins properties at laboratory scale.

3.1. Uniaxial compression test

Ten cylindrical rock samples were prepared according to the standard ASTM D4543-08,[44] and then tested under uniaxial compressive conditions using the standards included in ASTM D7012-04[45] at the Rock Mechanics laboratory of the University of Chile, Santiago, Chile. All samples were mapped in detail before and after testing, but only veins with thicknesses greater than 0.3 mm were described by their orientation, thickness, spatial position, length, roughness, and mineralogy [46]. In addition, veins are classified considering the most abundant mineral in their composition.

Table 1 presents the dimensions, weight and number of veins per type in the surface for each tested sample. The average sample has an aspect ratio (H/D) of 2.1 and a density of 2.82 [g/cm^3]. Quartz veins are dominant in all samples representing the 69% of the total number of veins, while anhydrite and chalcopyrite only represent the 25% and 6%, respectively. The distribution of hard infilling is presented in Fig. 3. An average vein is composed by more than 58% of hard infilling, which reflect the high content of quartz in the veins. This is consistent with the fact that most of all of the veins in the samples from CMET HW are composed by hard infilling.

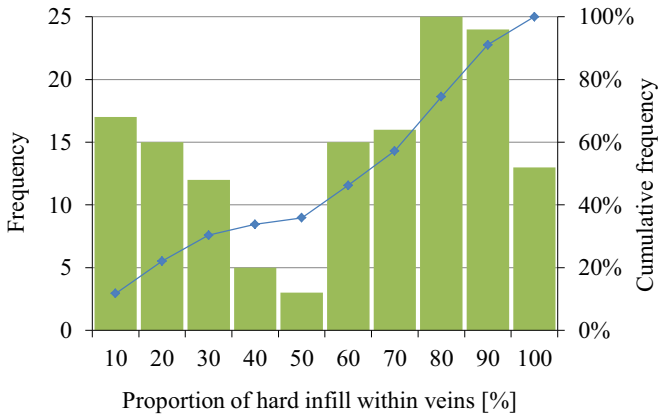

Fig. 3. Distribution of hard infilling observed within the veins of the samples.

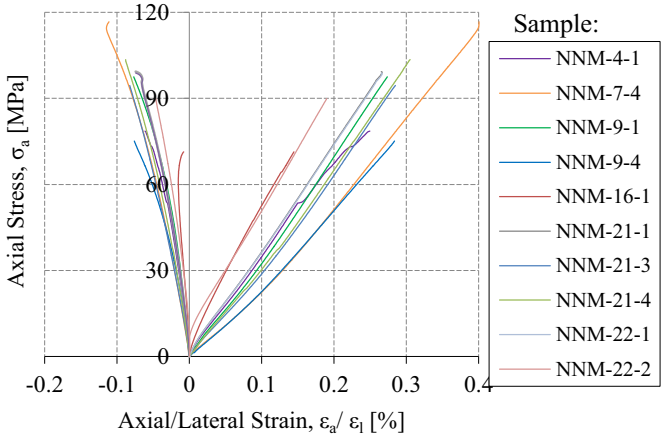

Fig. 4. Stress–strain curves measured in laboratory tests under uniaxial compression conditions on veined samples of CMET.

Table 2
Macro-parameters for the CMET lithology from laboratory tests.

Macro-parameters	
Young's modulus, E [GPa]	35.2 ± 5.4
Poisson's ratio, ν	0.22 ± 0.04
Crack initiation threshold, σ_{ci} [MPa]	39.8 ± 4.9
Crack damage threshold, σ_{cd} [MPa]	74.0 ± 11.2
Uniaxial compressive strength, UCS [MPa]	92.5 ± 14.0

Samples were tested using a servo-assisted press under controlled loading conditions with a constant speed of 0.3 [MPa/s]. Axial and lateral deformations were measured with strain gauges. Fig. 4 and Table 2 present the stress–strain curves and the average macro-parameters, respectively. These results will be used to calibrate and verify the performance of the SRM approach for representing the behavior of veined core-size samples.

In the laboratory samples, quartz veins dominates the failure process contrary to field observations of the caving progress,[3] where the rock mass of the primary copper ore fails mainly through pre-existing thick veins composed by less than 35% of hard minerals. At the laboratory scale, the most common mineral composition of the infill of failed veins was quartz, followed by anhydrite.[46] Fig. 5 presents five samples after testing. Eight of the samples showed a mixed mode of failure, sample NNM21-4 failed through the intact rock, and sample NNM9-4 failed along a single vein composed mainly of anhydrite ($>60\%$).

3.2. Intact rock parameters

The influence of the stockwork has changed the concept of the intact rock at the El Teniente mine, being described as a rock sample with veins of thickness less than 1 mm.[47] This has also an impact on the definition of failure of samples at the laboratory. Intact rock failure has been considered to represent not only samples failing by intact rock but also those samples that fail by both intact rock and veins.[48] Fig. 6 presents the scaling law of CMET samples obtained from UCS laboratory tests, considering only samples that failed by intact rock, and the adjusted relationship proposed in Ref. 49.

The macro-parameters of intact rock samples are adjusted using a database of 173 laboratory tests, standardizing values to 50-mm-diameter samples and considering an aspect ratio of $H/D = 2$.[50] They are presented in Table 3.

3.3. Veins parameters

Veins are very competent as a result of the occurrence of cemented infilling.[24] The composition of the infilling can be a unique type of mineral, or a mix of two or more predominant minerals such as anhydrite, bornite, chalcopyrite, quartz, molybdenite, biotite, chlorite, and pyrite. The contact between the infilling and the rock defines an interface, which is frequently the weakest link of the system though which the vein fails. Veins can also have heterogeneities, which may reduce the strength.

Fig. 5. Samples after being tested. Sample NNM09-4 failed though a single vein, sample NNM21-4 failed though intact rock, and samples NNM04-1, NNM16-1, and NNM22-2 failed through both veins and intact rock.

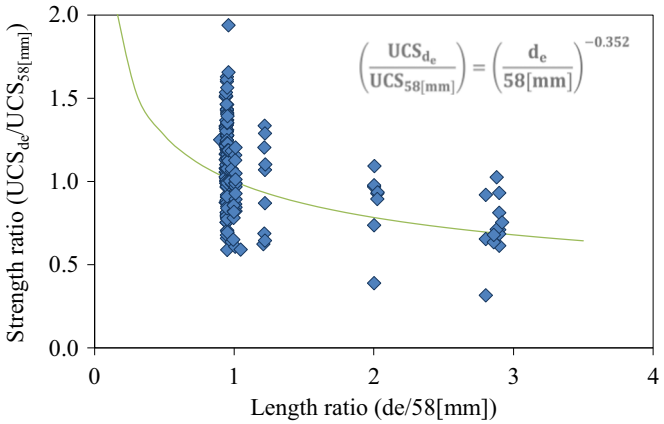

Fig. 6. UCS scale effect in samples of CMET unit.

In order to study the mechanical behavior of veins, a number of direct tension and direct shear tests were performed on samples containing isolated weak veins (both thin and thick) at the SP laboratory in Borås, Sweden.[22,51,52] Tables 4 and 5 present a summary of the direct tensile tests and the direct shear tests that failed through veins, respectively. From the direct shear tests, the normal (k_n) and shear stiffness (k_s) are estimated, considering veins characterized by thickness between 1.5 and 5.5 mm, and normal stresses between 5 and 10 MPa. These results indicate that $k_n < k_s$. This relationship is the opposite to that expected for open joints[53] or veins[24], and may be attributed to the testing equipment at SP, which may not be properly controlled during the loading–unloading cycles.

The shear behavior of veins is a combination of different phenomena and interactions such as roughness, wall strength, friction, and cohesion of the infill. The shear strength is essentially controlled by the roughness profile and the mineralogical content, in cases where the ratio between the thickness of the veins and amplitude of the roughness is lower than one. This is the condition of the primary mineralization rock mass at the El Teniente mine.[54] Table 6 presents the Mohr–Coulomb shear strength parameters of veins obtained from triaxial tests where the failure plane is clearly defined through only one vein.[22] The tested veins are characterized by a thickness between 0.1 and 2 mm, and lengths between 70 and 120 mm, and were tested under confinements between 20 and 110 [MPa]. The uniaxial compressive strength (UCS) of veins is estimated using the Mohr–Coulomb failure criterion:

$$UCS = c\left(\frac{2\cos\varphi}{1-\sin\varphi}\right) \quad (1)$$

The *UCS* of veins, which are composed mostly of quartz and anhydrite, is as high as the *UCS* of the intact rock.

4. Methodology

The methodology applied in this study consists on the calibration and assembly of the three components of the SRM model:

Table 4
Summary of direct tensile test results. All samples are from CMET lithology and fail through veins. [22, 54]

Mineral composition [%]	Diameter [mm]	Tensile strength, σ_t [MPa]
Py (66%)–Anh (17%)	63.2	1.0
Cpy (55%)–Chl (23%)	50.1	1.3
Cpy (77%)–Qz (20%)	50.1	1.0
Py (50%)–Bt (20%)	50.3	0.4

Table 5
Normal and shear stiffness of veins with thickness between 1.5 and 5.5 mm as a function of predominant minerals. Parameters are obtained from direct shear tests with confinements between 5 and 10 MPa.[22,54]

Type of vein (Texture)	Tests	Normal stiffness, k_n [MPa]	Shear stiffness, k_s [MPa]
Quartz (Granular)	7	20.5–65.8	17.0–116.2
Anhydrite (Granular)	2	31.4–35.9	47.1–52.6
Chalcopyrite (Massive)	13	8.02–73.0	26.6–129.1

Table 6
Shear strength parameters as a function of mineral composition of veins with thickness less than 2 mm. Parameters are obtained from triaxial tests with confinements between 20 and 110 MPa.[22]

Mineral composition (%)	Tests	Cohesion, c [MPa]	Friction angle, Φ [deg]	UCS [MPa]
Qz (40%) > Anh	5	42	34	158
Anh (70%) > Cpy (20%)	37	34	31	120
Anh (70%) > Qz (20%)	15	26	39	109
Cpy (70%) > Anh (30%)	26	19	38	78
Residual	12	0	40	–

DFN, BPM, and SJCM, in order to represent the mechanical behavior of core-size samples from the CMET HW lithology. The calibration of the SJCM and DFN is simplified to match just three types of veins: anhydrite, chalcopyrite, and quartz. Quartz veins represent hard infilling, while chalcopyrite and anhydrite represent intermediate hard infilling. The major challenge of the calibration of the SRM model is to properly determine the values of the micro-parameters in order to be consistent with laboratory tests.

Fig. 7 summarizes the main steps used in the numerical modeling. The first step is to generate a deterministic DFN representing explicitly the veins within each sample (Fig. 7a). Next, the calibration involves the selection of the micro-parameters by using an iterative process to reproduce the observed behavior of intact rock and veins at the laboratory scale. Initial micro-parameters are obtained by direct calibration of the behavior of the intact rock and veins observed in laboratory tests using samples of 50-mm diameter (initial simulations in Fig. 7b). Then, the micro-parameters are modified to improve the representation of the stress–strain curves and failure mode obtained from the uniaxial compressive tests for two samples (final calibration in Fig. 7b). General procedures for calibrating the enhanced BPM and the SJCM are

Table 3
Macro-parameters for CMET HW lithology normalized to 50-mm diameter.

Elastic parameters		Strength parameters						
		Laboratory tests average			Mohr–Coulomb criterion		Hoek–Brown criterion	
Young's modulus, E [GPa]	Poisson's ratio, ν	UCS [MPa]	Indirect tension, T_i [MPa]	Direct tension, T_d [MPa]	Cohesion, c [MPa]	Friction angle, φ [deg]	m_i	σ_c [MPa]
55	0.25	121	−13	−7.3	28.2	41.6	8.9	135.8

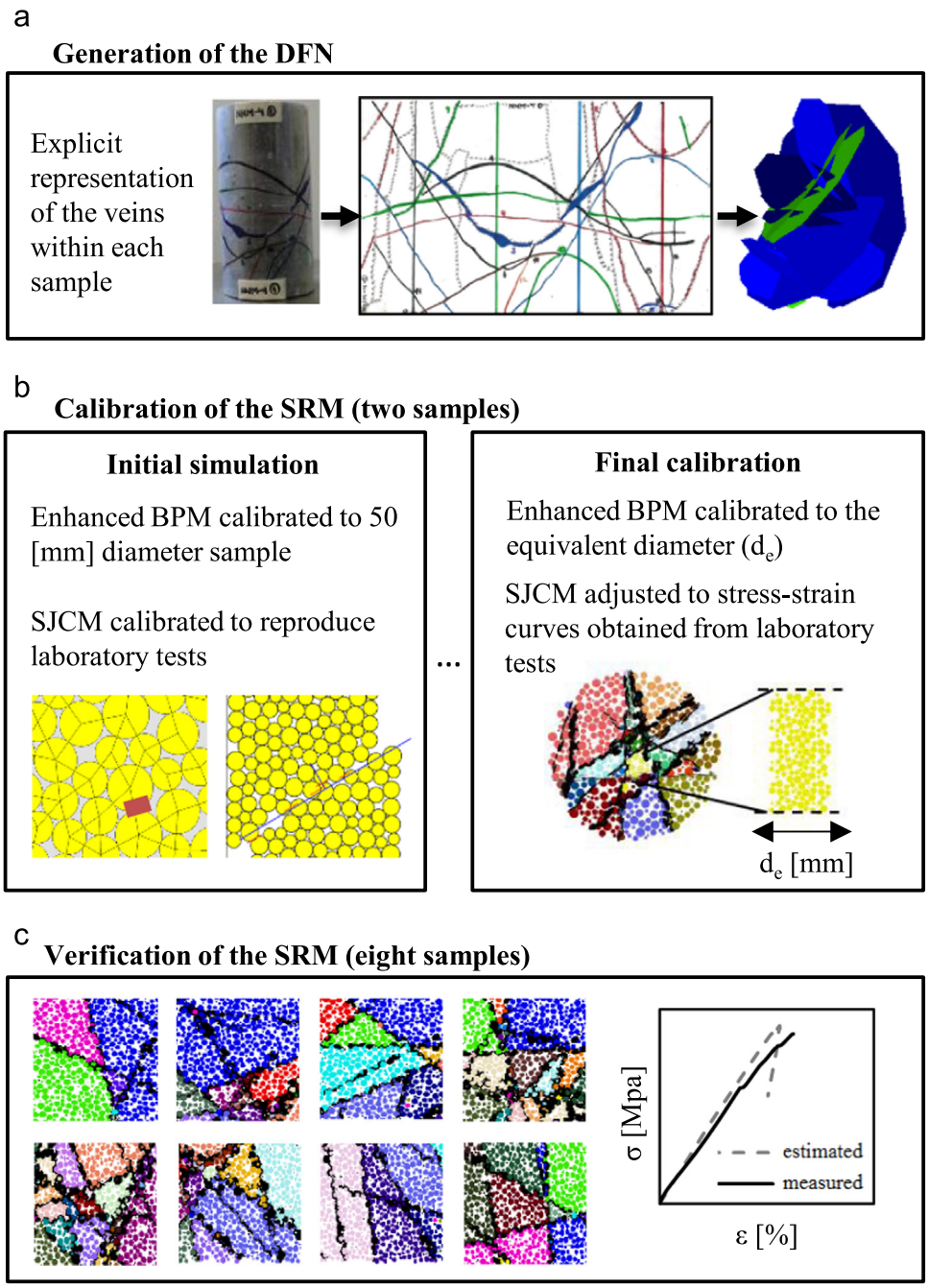

Fig. 7. Methodology of calibration and verification of the SRM model.

presented and used as the base for calibrating the SRM sample. Finally, the calibration is verified by testing eight samples under the same loading conditions (Fig. 7c).

4.1. Generation of a deterministic vein network (DFN)

The vein network is constructed deterministically in order to represent explicitly the veins within the sample using vein exposures on the surface of the core-size sample. The deterministic DFN construction involves the use of a CAD software to transform mapped veins from 2-D to 3-D. Fig. 8 shows the traces of veins on the surface of the sample NNM4-1 in 2D and 3D, and the resulting planes representing each vein. Veins in the model are simplified and represented as discs characterized by their orientation, position, radius, and mechanical properties. Internal veins can only be extrapolated, which is the same problem in both deterministic and stochastic realizations. Given that each vein has a different geometry and spatial location, each one has a different effect on the system. In a mine-scale model it is impossible to have the same level of detail than in a core-size sample, and consequently a large number of veins end up being neglected. But in case of samples with diameters of 50 mm, it is possible to capture most of the veins with reasonable certainty.

Joint hierarchy affects the order of insertion of veins.[14] The first family of veins inserted is continuous, while subsequent veins intersecting the first set are discontinuous, having asperities in the shared contacts at the intersections. Given that there is no clear evidence of joint hierarchy in the laboratory samples, the order of insertion is assumed to be from the higher to the lower stiffness of veins as was observed from the results of laboratory tests (Table 5).

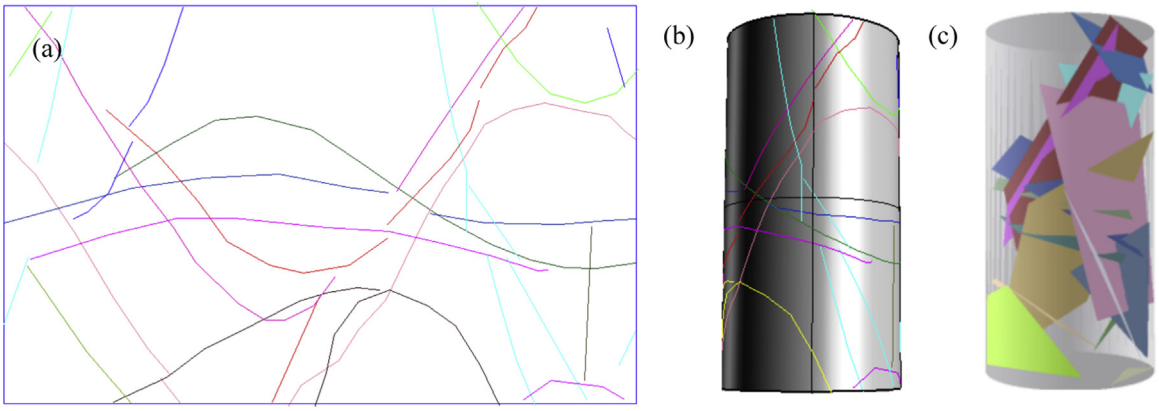

Fig. 8. DFN configuration based on: (a) the veins on the surface of sample NNM4-1, (b) sample veins traces in 2D, and (c) complete DFN in 3D with two sets of properties differentiated by color.

The implication is that, first the quartz veins are inserted in the synthetic sample, then the chalcopyrite veins, and finally the anhydrite veins.

4.2. Calibration of the BPM

To start the calibration of the BPM it is necessary to define the scale of the problem. The options are to calibrate the parameters of the model to a scale of 50 mm or to the average intact rock block size. The average intact rock block is defined by the equivalent diameter (d_e) as a function of the veins frequency (P_{10}) in three orthogonal directions from the generated DFNs using the following expression:

$$d_e=\sqrt{\frac{1}{P_{10}^x}\frac{1}{P_{10}^y}\frac{1}{P_{10}^z}} \quad (2)$$

Table 7 presents a summary of the average intact rock block and the total number of veins within each generated DFN. The equivalent diameter of the average block of intact rock is 10.7 mm.

Samples are generated following the procedure outlined in Ref. 30. Given the variability generated by the packing of particles when the synthetic samples are created, the calibration procedure has to match the average response of 20 synthetic samples to the required macroscopic behavior. In order to minimize resolution effects and simulation times, the particle size is such that approximately four particles are contained in the average block dimension. Four particles is the minimum resolution allowed to correctly represent the rock mass behavior.[55] Therefore, an average particle with a diameter of 2 mm is used. This resolution generates intact rock blocks of 402 and 30,603 particles for calibration samples with an equivalent diameter of 10.7 and 50 mm, respectively.

Table 7
Average intact rock block of each sample.

Sample	Total number of veins	Average block of intact rock, d_e [mm]
NNM-04–1	16	7.8
NNM-07–4	13	10.9
NNM-09–1	14	8.9
NNM-09–4	18	15.1
NNM-16–1	17	12.5
NNM-21–1	14	12.1
NNM-21–3	11	16.1
NNM-21–4	13	12.5
NNM-22–1	11	4.8
NNM-22–2	18	5.8
Min.	11	4.8
Max.	18	16.1
Mean	14.5	10.7
s.d.	2.6	3.8

The following assumptions are considered during the calibration of the BPM: (1) modeling does not include p-bricks, (2) samples are created using the same seed number and the parallel-bond refinement to match the macro-parameters of hard rock,[36] (3) the friction coefficient of the balls (μ) is 2.5, and (4) the radius multiplier is set equal to 1.0. The effect of the size distribution, defined by the ratio between maximum and minimum particle diameter (D_{max}/D_{min}), is fixed at 1.66.[30]

Many researchers have studied the calibration procedure for PFC applications and tried to establish the relationship between microscopic and macroscopic parameters using different optimization methods and stochastic techniques. Most of the studies are in PFC^{2D}[56,57] because of its simplicity, while works in PFC^{3D} are limited.[58–60] Based on these studies, the methodology used to calibrate the BPM is described in the following paragraphs.

The first step of the calibration procedure is to match the deformability parameters. Poisson's ratio is only controlled by the ratio between the normal and shear stiffness of parallel bonds ($\frac{\bar{k}^n}{\bar{k}^s}$), which is assumed to be equal to the ratio between the normal and shear stiffness of the contacts ($\frac{k^n}{k^s}$). Fig. 9a presents simulated stress–strain curves as a function of $\frac{\bar{k}^n}{\bar{k}^s}$. For values of $\frac{\bar{k}^n}{\bar{k}^s}$ higher than 2 the stress–strain curve presents a pre-peak softening behavior.

By using the enhanced BPM it is not possible to properly reproduce simultaneously a brittle behavior and a consistent Poisson's ratio value. In this study, it is assumed that the Poisson's ratio value is more influenced by the movement along veins than by the behavior of intact rock blocks. Therefore, the ratios $\frac{k^n}{k^s}$ and $\frac{\bar{k}^n}{\bar{k}^s}$ are fixed equal to 1.4. This value is considered to be the optimum for obtaining a brittle behavior in uniaxial compressive tests, but results in a low Poisson's ratio in comparison to the Poisson's ratio of the laboratory samples.

The macroscopic Young's modulus is controlled by the parallel bond Young's modulus ($\bar{E}_c$) and the ratio $\frac{\bar{k}^n}{\bar{k}^s}$. In order to better reproduce a brittle behavior, the value of the Young's modulus of the particles (E_c) has to be similar to $\bar{E}_c$ (Fig. 9b). The optimum value is set equal to $E_c=1.5\bar{E}_c$.

The next step is to calibrate the strength parameters. The tensile strength of the parallel bonds ($\bar{\sigma}_c$) is calibrated by matching the peak strength obtained from direct tensile tests. Next, the cohesion ($\bar{c}$) is calibrated by matching the peak strength of a uniaxial compressive test. Note that the standard deviations of the cohesion and normal bond strength are considered to be equal to 20%

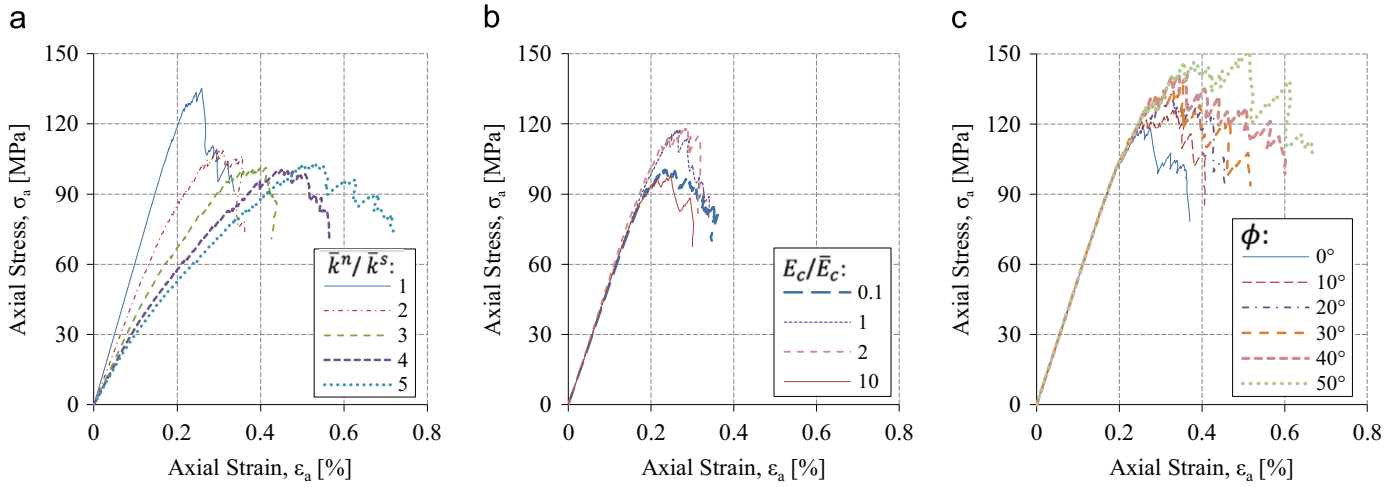

Fig. 9. Influence of different micro-parameters on the stress–strain curve, (a) the ratio between normal and shear stiffness, (b) Young's modulus of the particles, and (c) friction angle of parallel bonds.

of their mean values.[27]

To calibrate the friction angle of the parallel bonds ($\bar{\phi}$) it is necessary to simulate triaxial tests, which are not performed in the present study. As the friction angle of the parallel bonds increases, the uniaxial compressive strength increases and the post-peak behavior changes from brittle to ductile (Fig. 9c). Therefore, the friction angle is set equal to 0°.

4.3. Calibration of the SJCM

For the calibration of the SJCM the peak and residual friction angles are considered equal to 40°.[22] Adding vein dilation has shown to produce excessive rock dilation.[61] Therefore, the dilation angle is set equal to 0°. It is assumed that most of the rock mass dilation comes from blocks rotation and from the particles of relatively larger size.

To relate the micro-parameters of the SJCM with laboratory macro-parameters the smooth joint area ratio (A_{real}/A_{th}) is considered.[61] Vein planes are formed by numerous smooth-joint contacts in PFC^{3D}, which areas overlap each other. Therefore, the real discontinuity area (A_{real}) is larger than the theoretical one given by the geometry (A_{th}). Macro-parameters such as stiffness, cohesion, and tensile strength are estimated as the micro-parameter multiplied by the ratio A_{real}/A_{th}. The estimation of macro-parameters such as friction and dilation angles can be considered to be equal to the micro-parameters. Using this approach the error rate for estimate elastic macro-parameters is very low. However, for non-elastic macro-parameters the error can reach 10% in the estimation due to the complexity of the brittle behavior of the rock.

The dependency of the smooth joint area ratio (A_{real}/A_{th}) on the particle generation seed number and vein resolution was studied.[61] The resolution is defined as the number of particles along the vein length. After several simulations the following exponential fit was established between the ratio and vein resolution:

$$A_{ratio}=\frac{A_{real}}{A_{th}}=-1.122*e^{-\frac{x}{4.184}}+2.134 \quad (3)$$

where x is the vein resolution.

4.4. Calibration of the synthetic sample

4.4.1. Preliminary simulations

As a first approach, the enhanced BPM is calibrated to reproduce the behavior of a 50-mm-diameter sample of intact rock under uniaxial compressive and tensile conditions (target macro-parameters are presented in Table 3). At the same time, the SJCM is calibrated to directly represent direct shear and direct tension tests conducted on specimens containing infilled veins (target macro-parameters are presented in Tables 4–6). The micro-parameters calibrated using the methodology explained in Sections 4.2 and 4.3 are presented in Tables 8 and 9.

Fig. 10 presents the comparison between the macro-parameters obtained from laboratory and the synthetic tests. The Young's modulus, strength, and damage macro-parameters from simulations are lower than the expected values from the laboratory. Only Poisson's ratio shows acceptable values. These results can be explained by the fact that a complete microscopic modeling of the intact rock must consider the impact of flaws such as veins, healed joints, microscopic fractures, and pores, and none of them is explicitly represented in PFC^{3D}, which is not able to reproduce the scale effect of an intact rock sample or discontinuity.[30] These preliminary results suggest that the micro-parameters of the enhanced BPM and SJCM need to be adjusted to reproduce in a better manner the macroscopic behavior of the veined samples. Therefore, the micro-parameters are modified.

4.4.2. Final calibration

The micro-parameters of the BPM in the SRM sample are selected to match the behavior of scaled macro-parameters that represent the average intact rock block size.[14] Despite the absence of experimental tests for smaller diameters, scaling laws are used to obtain an estimate. When the scaling law presented in Fig. 6 is applied for the average 10.7-mm-diameter equivalent block, the scaled uniaxial compressive strength is almost the twice of the value of the 50-mm-diameter sample. Young's modulus and the Poisson's ratio are relatively scale-independent; therefore, no scale

Table 8
Micro-parameters calibrated for the enhanced BPM to a scale of 50 mm.

	Enhanced BPM micro-parameters	
Balls	Young's modulus, E_c [GPa]	133.5
	$\frac{k^n}{k^s}$	1.4
Parallel Bonds	Young's modulus, $\bar{E}_c$ [GPa]	89.0
	$\frac{\bar{k}^n}{\bar{k}^s}$	1.4
	Cohesion, $\bar{c}$ [MPa]	137.0 ± 27.4
	Tensile strength, $\bar{\sigma}_c$ [MPa]	15.4 ± 3.1

Table 9
Micro-parameters calibrated for SJCM to a scale of 50 mm.

SJCM micro-parameters	Anh	Cpy	Qz
Normal stiffness, $\bar{k}_n$ [GPa/m]	286	714	659
Shear stiffness, $\bar{k}_s$ [GPa/m]	29	71	66
Cohesion, c [MPa]	15	7	20
Tensile strength, σ_t [MPa]	7	3	9

effect is considered for them.[49,62] The calibrated BPM micro-parameters are presented in Table 10, and are obtained using the methodology presented in Section 4.2. The resulting macro-parameters are presented in Table 11, which are estimated with a maximum error of 0.23%.

Before start the calibration of the SJCM, the influence of the stiffness micro-parameters on the deformability macro-parameters is studied, using the sample NNM 7-4 and considering the same micro-parameters for all type of veins. Results are presented in Fig. 11. Large values of the strength micro-parameters of the SJCM are considered to obtain a better approximation. It is found that an increment of the shear stiffness ($\bar{k}_s$) increases Young's modulus and decreases Poisson's ratio for a given value of normal stiffness ($\bar{k}_n$), while an increment of $\bar{k}_n$ increases both elastic parameters. Similar trends in both macro-parameters (E, ν) are obtained using other DFNs. These relationships are used to estimate Young's modulus and Poisson's ratio as a function of $\bar{k}_n$ and $\bar{k}_s$.

The calibration of the SJCM considers the use of two samples: NNM7-4 and NNM16-1. The first step to adjust the deformability micro-parameters is to choose the stiffness micro-parameters ($\bar{k}_n$ and $\bar{k}_s$) of quartz and anhydrite veins in order to match Young's modulus and Poisson's ratio of the sample NNM 7-4. Then, chalcopyrite micro-parameters $\bar{k}_n$ and $\bar{k}_s$ are chosen to match the elastic response of the sample NNM 16-1. From laboratory tests the following relationship among the values of shear stiffness of the veins is considered: $k_s(\text{Qz}) > k_s(\text{Cpy}) > k_s(\text{Anh})$.

Table 10
Micro-parameters calibrated for the enhanced BPM to a scale of 10.7 mm.

	Enhanced BPM micro-parameters	
Balls	Young's modulus, E_c [GPa]	132.5
	$\frac{k^n}{k^s}$	1.4
Parallel bonds	Young's modulus, $\bar{E}_c$ [GPa]	88.3
	$\frac{\bar{k}^n}{\bar{k}^s}$	1.4
	Cohesion, $\bar{c}$ [MPa]	233.5 ± 46.7
	Tensile strength, $\bar{\sigma}_c$ [MPa]	27.2 ± 5.4

Table 11
Results of simulations for tensile and uniaxial tests of intact rock samples of 10.7-mm diameter.

Macro-parameters	
Young's modulus, E [GPa]	54.9 ± 5.2
Poisson's ratio, ν	0.09 ± 0.02
Crack initiation threshold, σ_{ci} [MPa]	70.4 ± 16.6
Crack damage threshold, σ_{cd} [MPa]	198.2 ± 29.9
Uniaxial compressive strength, UCS [MPa]	234.2 ± 34.1
Tensile strength, σ_t [MPa]	-14.1 ± 1.2

The next step to calibrate the micro-parameters considers choosing the strength macro-parameters to reproduce the global strength of both samples. For this purpose, it is considered the calibration of the strength parameters of the smooth-joints, which are set to a large value, and then are reduced until reach the global strength of samples NNM 7-4 and NNM 16-1. From field studies, it was concluded that the failure mode of veins forming blocks during caving at the El Teniente mine [3] is approximately 60 and 35% of shear and tension, respectively. This empirical evidence is

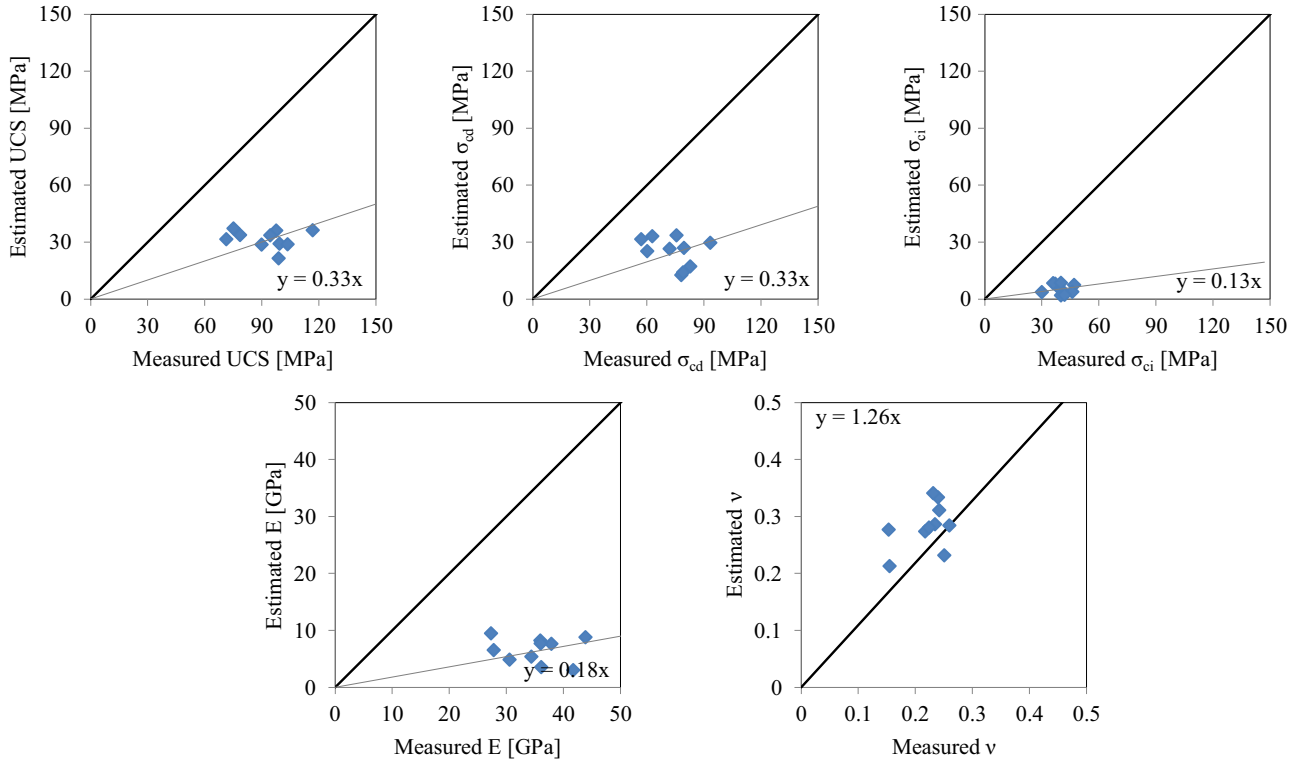

Fig. 10. Comparison of the macro-parameters obtained from the preliminary simulations using the SRM modeling and laboratory tests. Parameters are calibrated to represent UCS tests with no scale effect.

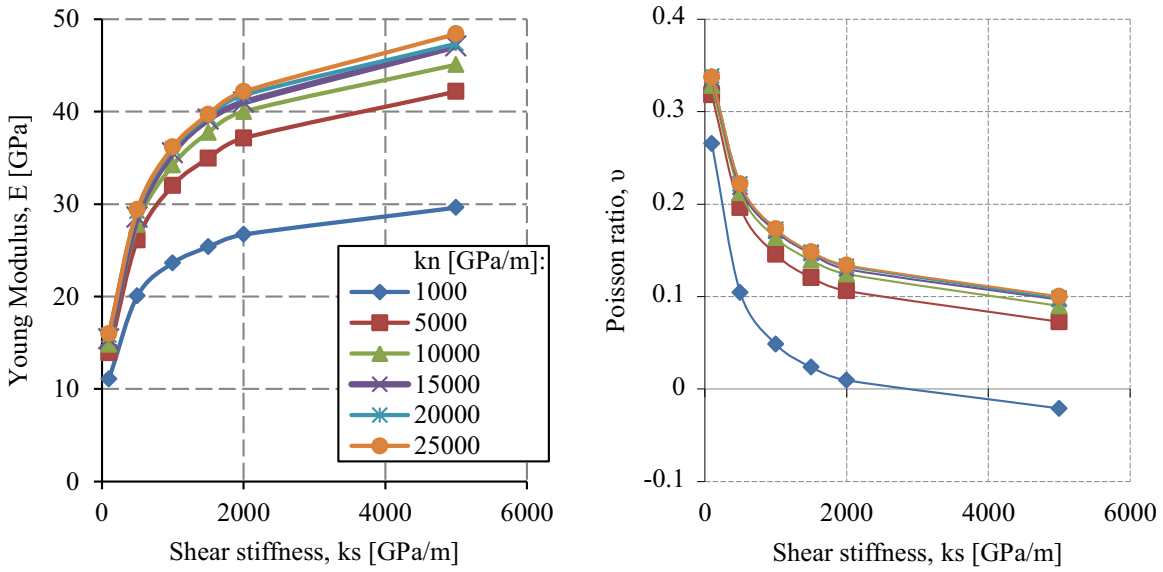

Fig. 11. Young's modulus and Poisson's ratio as a function of the shear stiffness of the SJCM. Results are obtained for sample NNM7-4, considering that all veins have the same composition.

used to complement the failure mode of the smooth-joints. For each type of vein, the ratio between the cohesion (c_b) and tensile strength (σ_t) is chosen to reproduce a fixed ratio between the number of smooth-joints contacts that have failed by shear and by tension as observed in the field. Finally, the cohesion of each type of vein (c_b) is chosen to reproduce the peak strength of the samples.

5. Results and discussions

Samples NNM7-4 and NNM16-1 are used to calibrate the micro-parameters necessary to define a SRM sample. The calibrated micro-parameters for the enhanced BPM and SJCM, which reproduce in a better manner a brittle post-peak behavior and capture the peak strength as well as the failure mode for both samples, are presented in Tables 10 and 12, respectively. The micro-parameters of the BPM and SJCM can be directly compared. The only exception is the stiffness micro-parameters of the BPM and SJCM, because the stiffness micro-parameters of the BPM are not explicitly defined. The normal stiffness micro-parameters of the BPM can be estimated as a function of the parallel bond moduli ($\bar{E}_c$) and the radii of the particles A and B sharing the bond ($R^{(A)}$ and $R^{(B)}$) by Eq. (4).[30] The shear stiffness micro-parameters can be estimated by the relationship $\bar{k}^s = \bar{k}^n/1.4$ as was previously defined during the calibration of the enhanced BPM. The radii of the particles are considered to be equal to the average radius of the particles. Therefore, the following values are obtained $\bar{k}^n = 44,012\left[\frac{\text{GPa}}{\text{m}}\right]$ and $\bar{k}^s = 31,437\left[\frac{\text{GPa}}{\text{m}}\right]$.

$$\bar{k}^n = \frac{\bar{E}_c}{R^{(A)} + R^{(B)}} \tag{4}$$

The stiffness and cohesion micro-parameters of the BPM result to be higher than the respective micro-parameters of the SJCM. In particular, the cohesion micro-parameter of the enhanced BPM results to be one order of magnitude higher than the cohesion micro-parameters of the SJCM. On the contrary, the resulting tensile strength micro-parameters of the SJCM are higher than the tensile strength micro-parameters of the BPM. If the tensile strength of quartz veins is decreased, the tensile strength of anhydrite and chalcopyrite becomes higher than that of quartz veins. Moreover, reducing the tensile strength of quartz veins to match the failure mode observed in laboratory tests in a better manner also resulted in a higher number of smooth-joint contacts that failed by tension, which is not representative of the laboratory tests.

The same comparison can be made with the macro-parameters of the intact rock presented in Table 11 and macro-parameters of veins. As simulations of veined samples involve long simulation times, the equivalent macro-parameters of the veins are estimated using the procedure presented in Section 4.3. Table 13 presents the results, considering as a reference a vein resolution of 22.6 particles across a 50-mm-diameter sample and the Mohr–Coulomb criterion to estimate the *UCS* of each type of vein. This analysis has two implications. The first one is that the strengths of both anhydrite and quartz veins are higher than that of the intact rock, which is consistent with the experimental results (Table 6). Also, a high tensile strength is obtained for all types of veins given that the ratio between the number of failed smooth-joint contacts by shear and tension is fixed and equal to field observations. If a higher UCS/σ_t ratio is imposed for the micro-parameters, smooth-joint contacts fail only by tension.[26] The second implication is that the macro-parameters of veins are three orders of magnitude higher than those obtained in laboratory tests. This can be caused

Table 12
Final micro-parameters calibrated for the SJCM.

SJCM micro-parameters	Anh	Cpy	Qz
Normal stiffness, $\bar{k}_n$ [GPa/m]	7,720	11,580	12,280
Shear stiffness, $\bar{k}_s$ [GPa/m]	386	579	614
Cohesion, c [MPa]	34.9	20.6	47.7
Tensile strength, σ_t [MPa]	33.8	20.1	46.5

Table 13
Macro-parameters estimated by Eq. (3) considering a vein resolution of 22.6 particles, 50 mm in diameter with the micro-parameters shown in Table 12.

Equivalent macro-parameters	Anh	Cpy	Qz
Normal stiffness, $\bar{k}_n$ [GPa/m]	16,435	24,653	26,143
Shear stiffness, $\bar{k}_s$ [GPa/m]	822	1233	1307
Cohesion, c [MPa]	74.3	43.9	101.6
Tensile strength, T_d [MPa]	71.0	42.8	99.0
Uniaxial compressive strength, *UCS* [MPa]	319	188	435

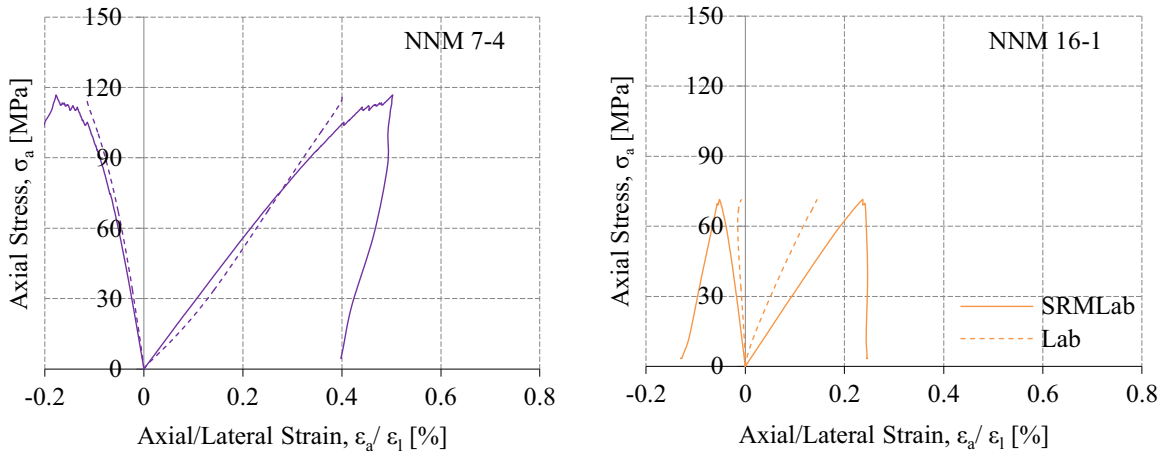

Fig. 12. Comparison between stress–strain curves from laboratory tests and SRM modeling (samples NNM7-4 and NNM16-1).

by an effect of the type of model used to represent veins like a smooth plane. Veins in the massive rock mass of the primary copper ore at El Teniente mine are extremely locked by the roughness profile,[54] which is implicitly considered by the current SJCM but is not considered in the laboratory tests used as initial step of the calibration.

Figs. 12 and 13 present the comparison between laboratory tests and SRM modeling for the stress–strain curves and failed veins mapped after testing the samples, respectively. Simulation of sample NNM7-4 matched in a better manner the Young's modulus, Poisson's ratio, and *UCS*, compared to simulation of sample NNM16-1. Both samples represent the post-peak behavior characteristic of a brittle rock. After being tested in the laboratory, the sample NNM7-4 presents a principal failure though a quartz vein (dip 83°) and partial failure though two veins, one composed mainly by quartz and the other one by anhydrite. However, the model reproduces a principal failure though an anhydrite vein and only partial failure by shear in two quartz veins. This situation is expected in the modeling given that anhydrite veins are weaker than quartz veins. On the other hand, in the laboratory test the sample NNM16-1 failed mainly through a chalcopyrite vein (dip 52°) and a quartz vein (dip 89°). After numerical modeling, the principal failure of this sample was through the same chalcopyrite vein that failed in the laboratory test and does not present relevant failure in quartz veins.

It is considered that the calibration is satisfactory as it reproduces the macroscopic behavior of the samples and matches the principal failure modes observed in laboratory tests. All macroparameters are constantly verified after each step until the calibration is accepted. To completely test the model not only the calibration is important. Therefore, the following subsections present the results of the verification simulations that represent eight samples from the same lithology.

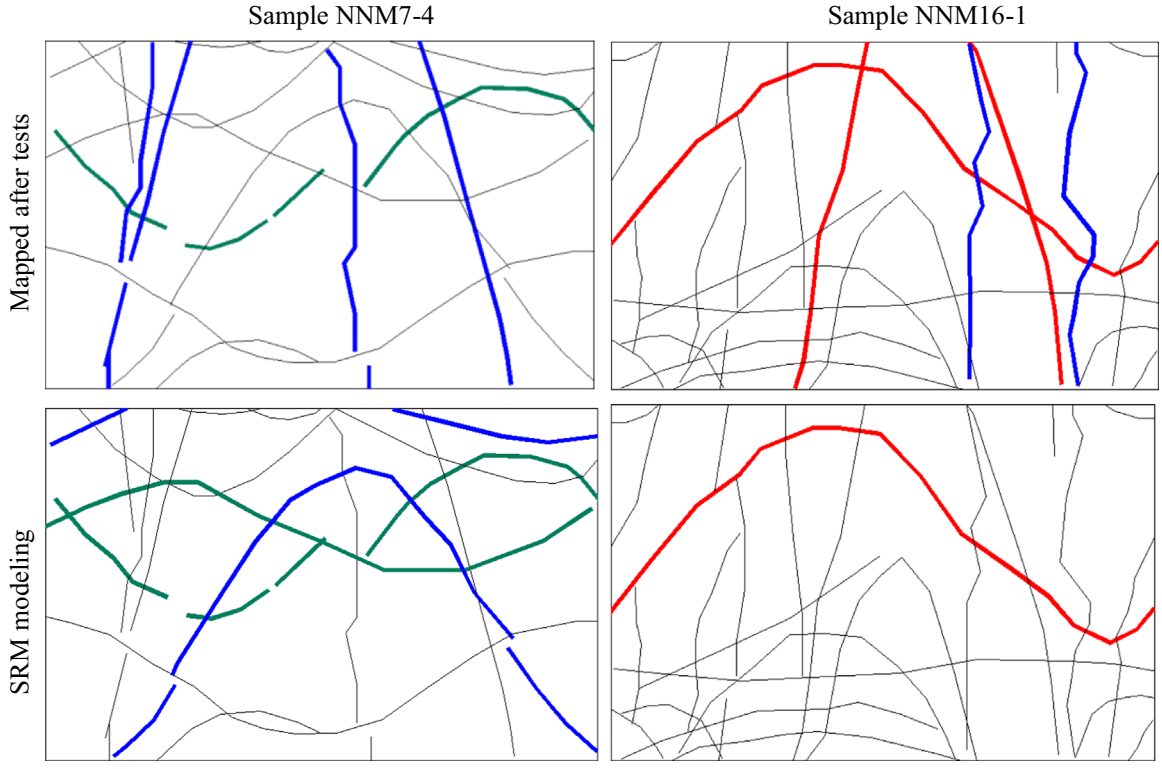

Fig. 13. Comparison between failed veins in laboratory tests and SRM modeling (quartz veins in blue, anhydrite veins in green, and chalcopyrite veins in red). (For interpretation of the references to color in this figure legend, the reader is referred to the web version of this article.)

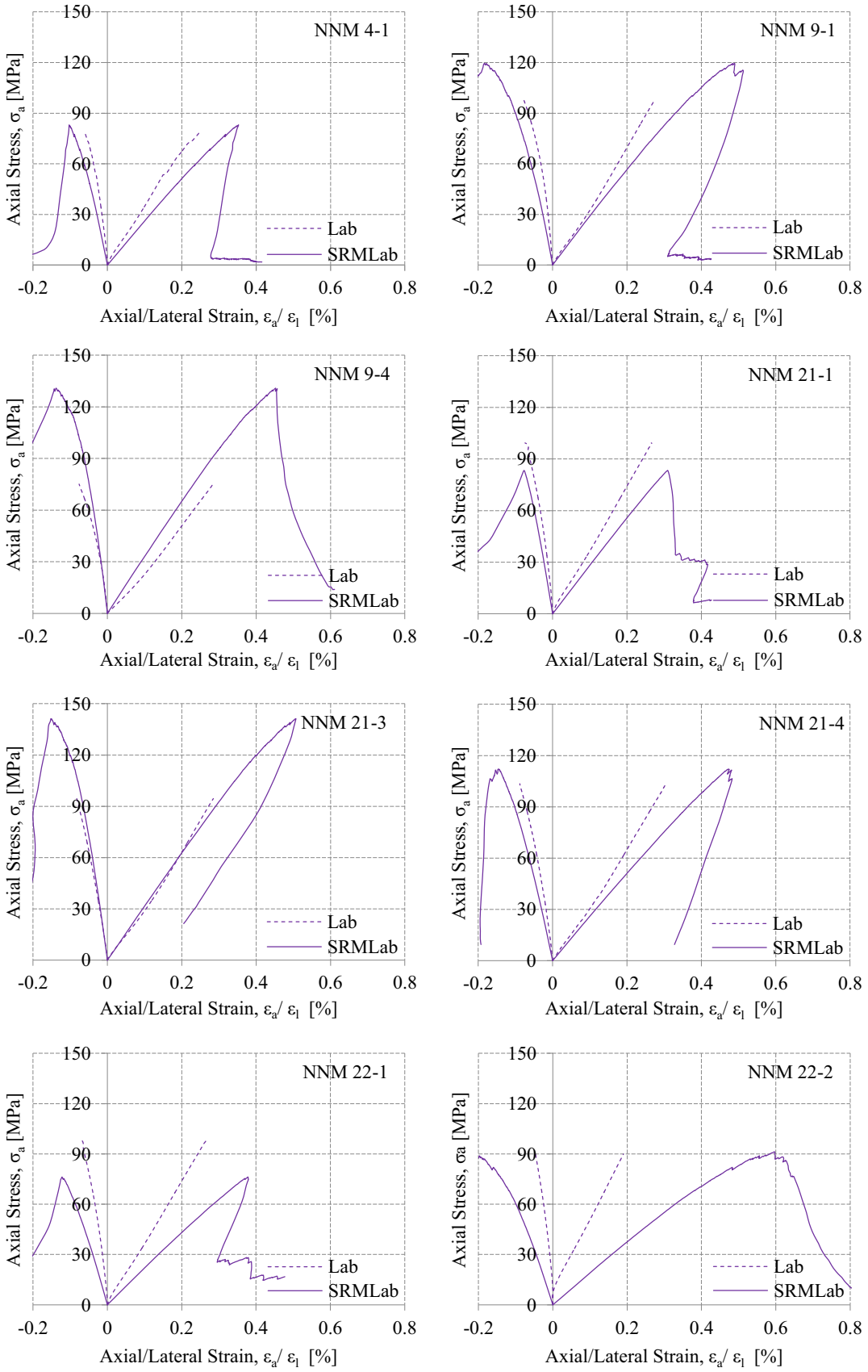

Fig. 14. Comparison between stress–strain curves from laboratory tests and SRM modeling (samples NNM4-1, NNM9-1, NNM9-4, NNM21-1, NNM21-3, NNM21-4, NNM22-1, and NNM22-2).

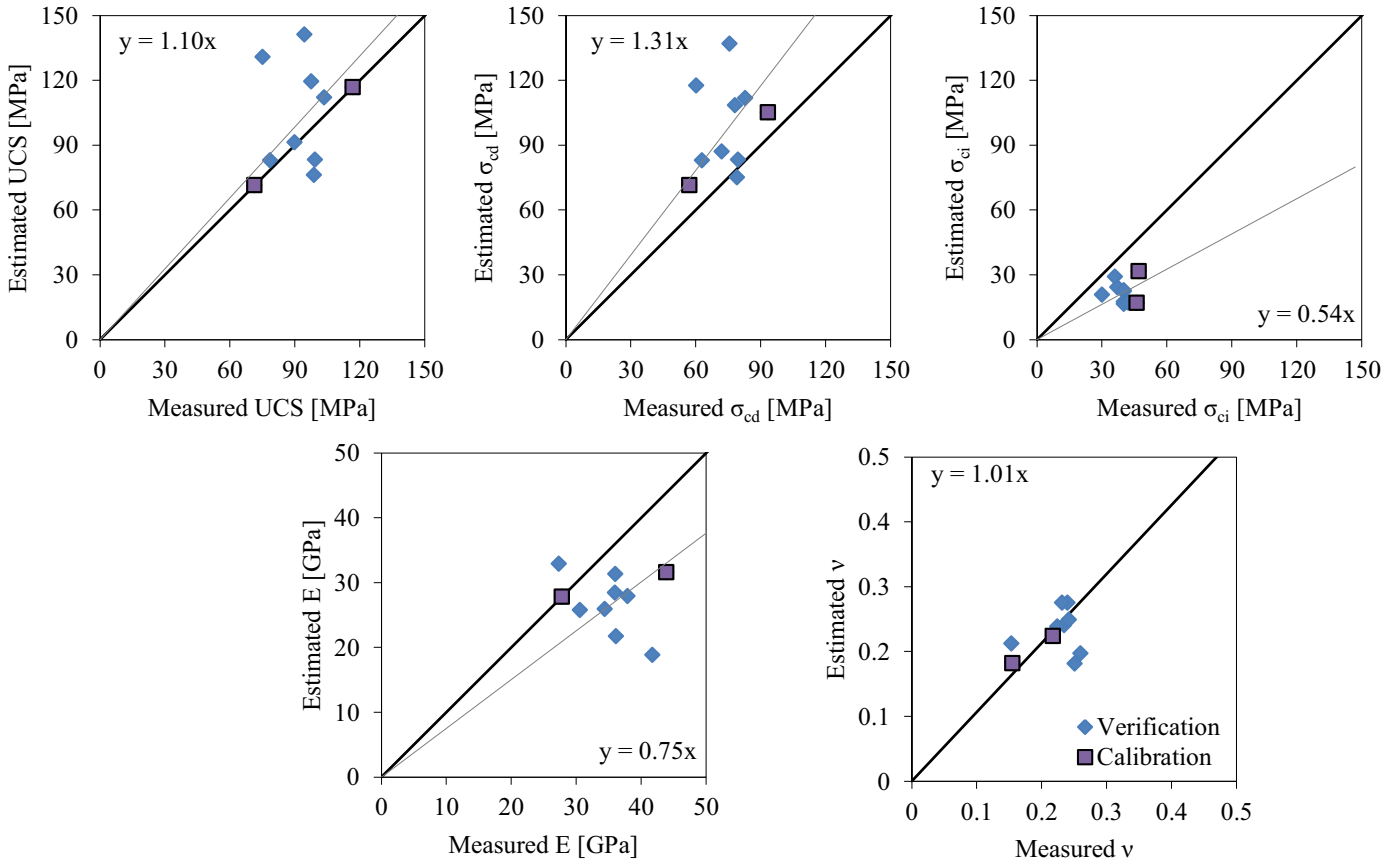

Fig. 15. Comparison of the calibrated macro-parameters obtained from the SRM modeling and laboratory tests.

5.1. Stress–strain curves and macro-parameters

Figs. 14 and 15 present the comparison between the laboratory and synthetic tests for the stress–strain curves and the macro-parameters, respectively. In general, the curves have an acceptable pre and post-peak behavior. None of simulated samples present a pre-peak softening behavior as the synthetic samples without veins do (Fig. 9). The conclusion is that the synthetic sample with veins is able to adequately reproduce lateral strains while keeping a brittle post-peak behavior, contrary to samples without veins. The best estimation is for the Poisson's ratio. The average simulation underestimates the uniaxial compressive strength (*UCS*) and the crack damage threshold (σ_{cd}), and overestimates Young's modulus (E) and the crack initiation threshold (σ_{ci}). It can be observed that these results represent in a better manner the laboratory tests compared with the previous simulations presented in Fig. 10. The final calibration considers three sets of veins instead of one, which is reflected in a higher variability of the macro-parameters.

The Mean Absolute Deviation (MAD) and the Mean Absolute Percentage Error (MAPE) are used to calculate the global error of the estimated macro-parameters in comparison to laboratory tests using the following expressions:

$$\text{Mean absolute deviation (MAD)} = \frac{\sum_1^n |x_{SRM} - x_{Lab}|}{n} \quad (5)$$

$$\text{Mean absolute percentage error (MAPE)} = \frac{\frac{\sum_1^n |x_{SRM} - x_{Lab}|}{x_{Lab}}}{n} \quad (6)$$

where x represents the macro-parameters *UCS*, *E*, and ν, and n is the number of simulations performed during the verification stage.

The MAD errors of *UCS*, *E*, and ν are 22 MPa, 10 GPa, and 0.04, respectively, while the MAPEs are 25%, 27% and 17%, respectively. This amount of error is within the acceptable range of conventional laboratory tests.

5.2. Failure mode

Synthetic samples failed mainly through the weakest veins, which are represented by anhydrite and chalcopyrite; contrary to what was observed in laboratory tests, where quartz veins dominated the failure. Failure though quartz veins can be explained by heterogeneities, which could reduce their strength. Moreover, anhydrite and chalcopyrite veins within the sample may be locked-in, generating high strength intact rock bridges and increasing the apparent strength of those veins. The model assumes that all quartz veins have the same characteristics, and the only difference among them is their orientation within the sample. If the micro-parameters had included heterogeneities or any other assumption based on mapping, the consideration of only quartz veins could have implied that 100 sets of micro-parameters would need to be defined instead of just one. The calibration of more than three sets of veins would mean a large number of iterations in order to calibrate all the parameters. This means that the problem will become impossible to solve, given that all veins should have been characterized in detail in order to be able to differentiate each of them.

6. Conclusions and recommendations

Commonly, open joints compose rock masses, but the primary copper ore at El Teniente mine is mainly composed of cemented

healed joints. With the use of a deterministic DFN it is possible to represent explicitly the vein network in a core-size sample. After simulating ten veined core-size samples of CMET lithology under uniaxial compressive conditions, it can be concluded that the SRM approach acceptably reproduces the peak strength, elastic parameters, and failure mode of the samples. In order to achieve the best combination of micro-parameters, the stress–strain curves and failure modes of the contacts in the model need to be checked. Otherwise, multiple combinations of micro-parameters could reproduce similar stress–strain curves with completely different failure modes [26].

In the El Teniente rock mass, the global rock mass strength is affected not only by the geometrical characteristics of the vein network but also by the strength of veins. In jointed rock masses, the geometrical characteristics affecting the rock mass strength are the fracture orientation and persistence regardless of the fracture intensity expressed as the fracture area per unit volume (P_{32}).[62] In order to simplify the problem, only three types of veins were defined. This assumption impacts on the variability of the resulting macro-parameters, as does the vein network. Anhydrite and chalcopyrite veins reduce the global strength, while quartz veins tend to increase it. If a large model is constructed, critical sets with similar characteristics should be defined, such as soft and hard veins,[27–29] instead of differentiating veins in function of their mineralogical composition.

The SRM technique has a high potential to represent the behavior of samples including both joints and veins. The main advantage of the technique is that it uses standard input data from laboratory tests and standard mapping techniques. However, there are still some limitations in the enhanced BPM, DFN and SJCM that need to be overcome to adequately represent the rock mass behavior. The most critical considerations are that Poisson's ratio of the intact rock cannot be matched at the same time that the stress–strain curve reproduces a brittle post-peak behavior, and that veins are modeled as smooth discs without considering the roughness profile explicitly. Another limitation is the run-time of the models. An increment from 50 to 150-mm-diameter samples means an increment from 30,000 to 826,000 particles using the same particle diameter. It was corroborated that running times increase exponentially as a function of the number of particles; therefore, it is not possible to simulate, with the same particle diameter, a large number of synthetic tests in order to evaluate the size effect in a reasonable simulation time.

A critical factor affecting the reliability of the model is the quality of the input data. Even though samples fail preferentially though veins in laboratory tests, they are the worst described component in the system. There is a lot of information available to describe the intact rock behavior of the El Teniente rock mass, but there are only few laboratory tests describing the behavior of weak and hard veins. One hundred and eleven samples containing infilled veins were included in this study, tested under different conditions, but only 12 of them represented quartz veins. The lack of data produces an overestimation of the quartz parameters. The few tests including quartz veins show that quartz increases the strength of the sample. However, it is also important to quantify the effect of factors reducing the strength of quartz veins such heterogeneities, which can have an impact in the variability of the strength. One assumption during the modeling made sets of quartz veins to have the highest strength in the system; consequently, it is not possible to reproduce the failure of larger percentages of quartz veins.

The geotechnical database of the El Teniente mine includes scaling laws of intact rock that were adjusted using larger sizes than the ones that represent the average intact rock block of the laboratory samples of this study. Therefore, macro-parameters have to be extrapolated. It is necessary to have available data describing both intact rock and vein behavior considering different mineral compositions and scales, and implement the scale effect in PFC^{3D}. Further studies need to be performed to improve the estimation of macro-parameters in order to establish scaling guidelines to be used as input data.

Acknowledgments

The authors acknowledge the El Teniente Division of Codelco Chile for giving permission to publish the data and for supporting this work, as well as Itasca Chile for providing the PFC^{3D} licenses that were used in this work. The authors would also like to acknowledge Mr Diego Diaz for mapping the samples included in this article.

This study was financed by API T10E202 of Codelco Chile (Contracts 4501127645 and 4501142662) and by FONDECYT Initiation into Research Grant no. 11110187.

References

1. Skewes M, Arevalo A, Floody R, Zuniga P, Stern C. The El Teniente megabreccia deposit: the world's largest deposit. In: Porter T, editor. *Super porphyry copper and gold deposits: a global perspective.* Adelaide, Australia: PGC Publishing; 2005. p. 83–114.
2. Garrido I., Riveros M., Cladouhos T., Espineira D., Allmendinger R. Modelo geológico estructural yacimiento El Teniente. In: *Proceedings of the VII Congreso Geológico Chileno*. Vol. 2. Concepción, Chile; 17–21 October 1994. , pp. 1533–1558.
3. Brzovic A, Villaescusa E. Rock mass characterization and assessment of block-forming geological discontinuities during caving of primary copper ore at the El Teniente mine, Chile. *Int J Rock Mech Min Sci.* 2007;44(4)565–583.
4. Cuadra P. Geocronología K–Ar del yacimiento El Teniente y áreas adyacentes. *Rev Geol Chile.* 1986;27:3–26.
5. A. Brzovic. *Characterization of primary copper ore for block caving at the El Teniente mine, Chile (Ph.D. thesis).* Australi: Curtin University of Technology; 2010.
6. Barton N, Lien R, Lunde J. Engineering classification of rock masses for the design of tunnel support. *Rock Mech.* 1974;6(4)189–236.
7. Hoek E, Kaiser P, Bawden W. *Support of underground excavations in hard rock. Rotterdam.* Balkema; 1997.
8. Laubscher D. Planning mass mining operations. In: Hudson J, editor. *Comprehensive Rock Engineering: Principles, Practice and Projects, Vol. 2*. Oxford: Pergamon Press; 1993. p. 547–583.
9. D. Laubscher, J. Jakubec. The MRMR rock mass classification system for jointed rock masses. In: Littleton C, editor. *Underground mining methods: engineering fundamental and international case studies.* Society for Mining, Metallurgy, and Exploration, Inc.; 2011. p. 475–481.
10. Itasca Consulting Group. *PFC3D – Particle Flow Code in 3 Dimensions*, Version 4.0. Minneapolis; 2008.
11. Itasca Consulting Group. *SRMLab*, Version 1.7. Minneapolis; 2012.
12. Cundall P, Strack O. A discrete numerical model for granular assemblies. *Geotechnique.* 1979;29(1)47–65.
13. Pierce M., Mas Ivars D., Cundall P., Potyondy D. A synthetic rock mass model for jointed rock. In: *Proceedings of the 1st Canada–U.S. Rrock Mechanics Symposium*. Vancouver, Canada; 27–31 May 2007. pp. 341–349.
14. Mas Ivars D. *Bonded Particle Model for Jointed Rock Mass (Ph.D. thesis).* Stockholm, Sweden: Royal Institute of Technology (KTH); 2010.
15. Mas Ivars D, Pierce M, Darcel C, Reyes-Montes J, Potyondy D, Young P, Cundall P. The Synthetic Rock Mass approach for jointed rock mass modeling. *Int. J. Rock. Mech. Min. Sci..* 2011;48(2)219–244.
16. Reyes-Montes J, Pettitt W, Young R. Validation of a synthetic rock mass model using excavation induced microseismicity. In: *Proceedings of the 1st Canada–U.S. Rock Mechanics Symposium.* Vol 1. Vancouver, Canada; 27–31 May 2007. p. 365–436.
17. Esmaieli K, Hadjigeorgiou J, Grenon M. Estimation of synthetic rock mass strength accounting for sample size. In: *Proceedings of the International Conference on Rock Joints and Jointed Rock Masses*. Tucson, United States; 4–11 January 2009 (Paper no. 1034).
18. Cundall P, Pierce M, Mas Ivars D. Quantifying the size effect of rock mass strength. In: *Proceedings of the 1st Southern Hemisphere International Rock Mechanics Symposium (SHIRMS).* Perth, Australia; 16–19 September 2008. pp. 3–15.
19. Esmaieli K, Hadjigeorgiou J, Grenon M. Estimating geometrical and mechanical REV based on synthetic rock mass models at Brunswick Mine. *Int J Rock Mech Min Sci.* 2010;47(6)915–926.
20. Sainsbury B, Pierce M, Mas Ivars D. Analysis of Caving Behaviour Using a Synthetic Rock Mass – Ubiquitous Joint Rock Mass Modelling Technique. In: *Proceedings of the 1st Southern Hemisphere International Rock Mechanics Symposium*

(SHIRMS). Vol. 1. Perth, Australia; 16–19 September 2008. pp. 243–254.
21. Bahaaddini M, Sharrock G, Hebblewhite BK. Numerical investigation of the effect of joint geometrical parameters on the mechanical properties of a non-persistent jointed rock mass under uniaxial compression. *Comput Geotech.* 2013;49:206–225.
22. De los Santos C. Efecto de la Mineralogía, Alteración, y Geometría en la Resistencia Mecánica de las Vetillas, Mina El Teniente, Región del Libertador Bernardo O'Higgins, Chile. Geologist thesis. Universidad de Concepción, Concepción, Chile; 2011.
23. Vallejos J. *Técnica de modelamiento numérico de macizos rocosos sintéticos*. Universidad de Chile report to División El Teniente, Codelco Chile. API T10E202 project; Santiago, Chile; 2012. SRM-ET-Uch-06.
24. Karzulovic A. Propiedades geomecánicas de estructuras en roca primaria. División El Teniente, Codelco Chile, Internal report. Rancagua Chile; 2001. Dt-cg-01-003.
25. Ramírez F. *Simulación del comportamiento geomecánico de las vetillas del Yacimiento El Teniente mediante PFC3D (Geologist thesis).* Santiago, Chile: Universidad de Chile; 2012.
26. Suzuki K. *Aplicación de la técnica Synthetic Rock Mass a escala de laboratorio (Master's thesis).* Santiago, Chile: Universidad de Chile; 2013.
27. Vallejos J., Brzovic A., Lopez C., Bouzeran L., Mas Ivars D. Application of the Synthetic Rock Mass approach to characterize rock mass behavior at the El Teniente Mine, Chile. In: *Proceedings of the 3rd International FLAC/DEM Symposium*. Hangzhou, China; 22–24 October 2013. Paper: 07-02.
28. Brzovic A, Schachter P, de los Santos C, Vallejos J, Mas Ivars D. Characterization and Synthetic Simulations to Determine Rock Mass Behaviour at the El Teniente Mine, Chile. Part I. In: *Proceedings of the 3rd International Symposium on Block and Sublevel Caving*. Santiago, Chile; 5–6 June 2014. pp. 171–178.
29. Vallejos J, Suzuki K, Brzovic A, Mas Ivars D. Characterization and Synthetic Simulations to Determine Rock Mass Behaviour at the El Teniente Mine, Chile. Part II. In: *Proceedings of the 3rd International Symposium on Block and Sublevel Caving*. Santiago, Chile; 5–6 June 2014. pp. 179–188.
30. Potyondy D, Cundall P. A bonded-particle model for rock. *Int J Rock Mech Min Sci.* 2004;41(8)1329–1364.
31. Mas Ivars D, Potyondy D, Pierce M, Cundall P. The smooth-joint contact model. In: *Proceedings of the 8th World Congress on Computational Mechanics/5th European Congress on Computational Mechanics and Applied Science and Engineering*. Venice, Italy; 30 June–4 July 2008 (Paper a2735).
32. Diederichs M. *Instability of hard rockmasses: the role of tensile damage and relaxation (PhD thesis).* Canada: University of Waterloo; 1999.
33. Schöpfer M, Abe S, Childs C, Walsh J. The impact of porosity and crack density on the elasticity, strength and friction of cohesive granular materials: insights from DEM modelling. *Int J Rock Mech Min Sci.* 2009;46(2)250–261.
34. Ding X, Zhang L, Zhu H, Zhang Q. Effect of Model Scale and particle size distribution on PFC3D simulation results. *Rock Mech Rock Eng.* 2013:1–18.
35. Cho N, Martin C, Sego D. A clumped particle model for rock. *Int J Rock Mech Min Sci.* 2007;44:997–1010.
36. Potyondy D. Parallel-bond refinements to match macroproperties of hard rock. In: *Proceedings of the 2nd International FLAC/DEM Symposium*. Melbourne, Australia; 14-16 February 2011. Paper: 08–04.
37. Potyondy D. The bonded-particle model as a tool for rock mechanics research and application: current trends and future directions. In: *Proceedings of the 7th Asian Rock Mechanics Symposium*. Seoul Korea; 15–19 October 2012. pp. 73–105.
38. Potyondy D. A flat-jointed bonded-particle material for hard rock. In: *Proceedings of the 46th U.S. Rock Mechanics/Geomechanics Symposium, American Rock Mechanics Association*. Chicago, United States; 24–27 June 2012. pp. 1510–1520.
39. Park J, Song J. Numerical simulation of a direct shear test on a rock joint using a bonded-particle model. *Int J Rock Mech Min Sci.* 2009;46(8)1315–1328.
40. Chiu C, Wang T, Weng M, Huang T. Modeling the anisotropic behavior of jointed rock mass using a modified smooth-joint model. *Int J Rock Mech Min Sci.* 2013;62:14–22.
41. Bahaaddini M, Sharrock G, Hebblewhite B. Numerical direct shear tests to model the shear behaviour of rock joints. *Comput Geotech.* 2013;51:101–115.
42. Lambert C, Coll C. Discrete modeling of rock joints with a smooth-joint contact model. *J Rock Mech Geotech Eng.* 2014;6(1)1–12.
43. Lazzari E, Johansson F, Mas Ivars D, Sánchez Juncal A. Advances, current limitations and future requirements for a numerical shear box for rock joints using PFC2D. In: *Proceedings of the Eurock 2014 (ISRM European Rock Mechanics Symposium)*. Vigo, Spain; 27–29 May 2014. pp. 763–768.
44. ASTM D454.3–08. Standard Practices for Preparing Rock Core as Cylindrical Test Specimens and Verifying Conformance to Dimensional and Shape Tolerances; 2008.
45. ASTM D701.2–04. Standard Test Method for Compressive Strength and Elastic Moduli of Intact Rock Core Specimens Under Varying States of Stress and Temperatures; 2004.
46. Rebolledo S. *Descripción geológica de probetas pre y post ensayos – Probetas de 50 [mm] diámetro*. Universidad de Chile report to División El Teniente, Codelco Chile. API T10E202 Project, Santiago Chile; 2012.
47. Marambio F, Pereira J, Russo A. Caracterización De Las Propiedades Geotécnicas De Las Andesitas De La Mina, Yacimiento El Teniente, Chile Central. In: *Proceedings of the IX Congreso Geológico Chileno*. Vol. 1. Puerto Varas, Chile; 31 July–4 August 2000. pp. 279–82.
48. Pereira J, Russo A. *Estudio propiedades geotécnicas proyectos Diablo Regimiento y Pipa Norte*. Superintendencia Geología, División El Teniente, Codelco Chile, Internal report; 2000, GL-183/00.
49. Yoshinaka R, Osada M, Park H, Sasaki T, Sasaki K. Practical determination of mechanical design parameters of intact rock considering scale effect. *Eng Geol.* 2008;96(3/4)173–186.
50. Quezada O. *Antecedentes geológicos y geotécnicos del área a incorporar el año* 2012 (PO). División El Teniente, Codelco Chile, Internal report; 2011, SGL-I-072-2011.
51. Flansbjer M. *Direct shear and tensile tests of unbroken rock joints*. SP Technical Research Institute of Sweden report to División El Teniente, Codelco Chile. Borås, Sweden; 2010. SP laboratory report reference PX00650.
52. Jacobsson L, Flansbjer M, Brzovic A, de los Santos C. Direct shear and tensile test on cemented healed joints from El Teniente Mine, Chile. In: *Proceedings of the 12th ISRM Congress*. Beijing, China; 16–21 October 2011.
53. Bandis S. Engineering properties and characterization of rock discontinuities. In: Hudson J, editor. *Comprehensive Rock Engineering: Principles, Practice and Projects, Vol. 2*. Oxford: Pergamon Press; 1993. p. 18–155.
54. Díaz D, Brzovic A. 2D and 3D Roughness profile of weak stockwork veins at mine scale in the El Teniente mine. In: *Proceedings of the 3rd International Seminar on Geology for the Mining Industry (Geomin).* Santiago, Chile 24–26 July 2013.
55. Darcel C, Bouzeran L. *Jointed rock mass sensitivity to DFN properties – Intensive SRM Study and Comparison to Classical use of GSI Indexes*. Itasca Consultants S.A. S France, Internal Report; 2011, 11R–039.
56 Fakhimi A, Villegas T. Application of dimensional analysis in calibration of a discrete element model for rock deformation and fracture. *Rock Mech Rock Eng.* 2007;40(2)193–211.
57. Yoon J. Application of experimental design and optimization to PFC model calibration in uniaxial compression simulation. *Int J Rock Mech Min Sci.* 2007;44(6)871–889.
58. Tawadrous A, De Gagné D, Pierce M, Mas Ivars D. Prediction of uniaxial compression PFC3D model micro-properties using artificial neural networks. *Int J Numer Anal Met.* 2009;33(18)1953–1962.
59. Wang Y, Tonon F. Modeling Lac du Bonnet granite using a discrete element model. *Int J Rock Mech Min Sci.* 2009;46(7)1124–1135.
60. Kulatilake P, Malama B, Wang J. Physical and particle flow modeling of jointed rock block behavior under uniaxial loading. *Int J Rock Mech Min Sci.* 2001;38(5)641–657.
61. Mas Ivars D, Bouzeran L, Le Goc R, Darcel C. Final report on Synthetic Rock Mass (SRM) Fragmentation Analysis – El Teniente, March, 2013. *Itasca Consultants AB Report to División El Teniente*, Codelco Chile. API T10E202 project; 2013.
62. Martin C, Lun Y, Lan H. Scale effects in a synthetic rock mass. In: Zhou Y, editor. *Harmonizing Rock Engineering and the Environment.* CRC Press; 2011. p. 257.